

GNSS Precise Point Positioning in Cislunar Space: A Study on Regularized Least Squares and Availability

Original

GNSS Precise Point Positioning in Cislunar Space: A Study on Regularized Least Squares and Availability / Vouch, Oliviero; Morichi, Luca; Zocca, Simone; Minetto, Alex; Dosis, Fabio. - ELETTRONICO. - (2025), pp. 1014-1025. (IEEE/ION Position, Location and Navigation Symposium. 2025 Salt Lake City (USA) 28 April 2025 - 01 May 2025) [10.1109/plans61210.2025.11028416].

Availability:

This version is available at: 11583/3001149 since: 2025-06-20T08:05:03Z

Publisher:

IEEE

Published

DOI:10.1109/plans61210.2025.11028416






Terms of use:

This article is made available under terms and conditions as specified in the corresponding bibliographic description in the repository

Publisher copyright

(Article begins on next page)

GNSS Precise Point Positioning in Cislunar Space: A Study on Regularized Least Squares and Availability

Oliviero Vouch , Luca Morichi , Simone Zocca , Alex Minetto , Fabio Dovis 

Politecnico di Torino

Dept. of Electronics & Telecommunications (DET)

Turin, Italy

{oliviero.vouch, luca.morichi, simone.zocca, alex.minetto, fabio.dovis}@polito.it

Abstract—The ongoing Lunar GNSS Receiver Experiment (LuGRE) mission is demonstrating that Global Navigation Satellite System (GNSS) can be a major enabler for radionavigation in cislunar space and on the Moon, offering a complementary solution to ground-based tracking infrastructures. However, cislunar Orbit Determination (OD) and timing with GNSS signals remains challenging due to severe pathloss effects, frequent side lobe receptions, and degraded satellite geometry. This study evaluates a single-frequency precise point positioning (SF-PPP) approach for kinematic OD, leveraging the group and phase ionospheric calibration (GRAPHIC) model to process undifferenced code and phase observations. The method incorporates Tikhonov regularization within a batch nonlinear least square (LS) estimator to tackle the ill-conditioning caused by the inherent rank deficiency of the positioning model. The algorithm is assessed through post-processing of raw GNSS observables collected during a hardware-in-the-loop (HIL) test, simulating representative LuGRE payload operations. Results show that the proposed regularized estimator ensures more than 89% solution availability in most of the scenarios and achieves sub-kilometer positioning accuracy, even in scenarios with insufficient measurement redundancy.

Index Terms—Global navigation satellite systems, Radio navigation, Space exploration, Kinematic orbit determination, Least squares approximations, Tikhonov method.

I. INTRODUCTION

The new space era is reshaping space exploration, with increasing investments from both public and private sectors driving the development of the Lunar Gateway and permanent lunar bases. These infrastructures serve as key stepping stones for future deep space missions [1]. A fundamental aspect of this expansion is the need for reliable Positioning, Navigation, and Timing (PNT) services [2]. While dedicated systems such as LunaNet [3] are being designed to provide autonomous navigation solutions, there is growing interest in leveraging Global Navigation Satellite Systems (GNSSs) as a complementary source of navigation data in the cislunar space.

Traditionally, navigation beyond Earth orbit has relied on ground-based tracking networks such as NASA’s Deep Space Network (DSN) and ESA’s Estrack. However, the increasing number of deep space missions is pushing these systems to their operational limits. As an alternative, the possibility of equipping a spacecraft (S/C) with a GNSS receiver is

being investigated for Orbit Determination (OD) and timing leveraging signals originally designed to serve terrestrial users.

GNSS-based OD in the cislunar space poses several technological challenges. One of the most critical issues is the severe free-space path loss, which significantly attenuates signals over long distances. Moreover, S/C in this region primarily receive GNSS signals through secondary lobes, resulting in weaker and noisier observations compared to those used in terrestrial satellite navigation. However, it should be noted that the ability to acquire and track such degraded signals ultimately depends on the design and sensitivity of the onboard receiver. Additional factors, such as Earth occultation and the unfavorable geometric distribution of the transmitting satellites, further degrade the conditioning of the multilateration problem. Despite these limitations, multiple studies have demonstrated the feasibility of OD with GNSS signals in Moon transfer orbit (MTO) and at the Moon [4], [5]. More recently, the Lunar GNSS Receiver Experiment (LuGRE) [6], [7], currently onboard the Firefly Blue Ghost Mission 1 (BGM1) lander, has provided in-orbit validation of GNSS-based navigation in the cislunar region. By successfully acquiring and tracking signals from both GPS and Galileo constellations, LuGRE is demonstrating that GNSS can support future lunar and deep-space navigation infrastructures, even under extreme operational conditions far beyond its regulated use within the Space Service Volume (SSV) [8].

Building on this framework, this study investigates the performance of a single frequency (SF)-Precise Point Positioning (PPP) model [9] for kinematic OD in cislunar space and on the Moon’s surface. The term PPP is used here to align with the GNSS literature, where it typically refers to an absolute positioning model that combines both code and carrier-phase measurements. However, it is important to note that terrestrial PPP and its application in the cislunar environment, particularly onboard OD, differ substantially.

First, onboard OD in cislunar space relies on GNSS broadcast ephemerides or, at best, ultra-rapid products. In contrast, the precise orbit and clock products provided by the International GNSS Service (IGS) analysis centers are only available for post-processing. Real-time precise correction services, on

the other hand, are currently being considered exclusively for terrestrial users and are offered on a commercial basis. Although the use of ultra-rapid products is technically feasible, it implies a stronger dependency on the ground segment. Moreover, the benefit of improved orbit accuracy may be negligible compared to the challenges posed by processing noisy measurements due to weak signal tracking. Therefore, point positioning models in the cislunar domain should not be evaluated against centimeter-level performance expectations typical of terrestrial PPP.

Another crucial aspect is the availability of atmospheric correction models, such as those for tropospheric and ionospheric delays. To the best of the authors' knowledge, such models are currently not available for a space users. To mitigate the impact of ionospheric delay, this work adopts a SF approach based on the group and phase ionospheric calibration (GRAPHIC) method. The proposed method uses undifferenced code and phase observations combined with the GRAPHIC model [10], formulating the positioning problem as a batch nonlinear least squares estimation, regularized via the Tikhonov method. The regularization term, incorporating both a regularization matrix and an a-priori estimate of the receiver state, mitigates ill-conditioning due to the inherent rank deficiency of the model Jacobian. The regularized positioning algorithm exploits the generalized singular value decomposition (GSVD) framework [11] to accommodate both overdetermined and underdetermined structures, thus ensuring robustness to variable measurement redundancy across different batches.

The proposed algorithm is evaluated through post-processing of raw multi-band GPS/Galileo observables generated by the LuGRE receiver in a hardware-in-the-loop (HIL) test, simulating representative payload operations across various mission phases. The analysis focuses on Position, Velocity, Timing (PVT) solution availability and positioning performance, considering different satellite visibility constraints and uncertainties on the a-priori estimate of the receiver state.

The article is organized as follows. Section II provides an overview of the SF-PPP model and the nonlinear least square (LS) approach for GNSS positioning. Section III describes the methodology, including the regularization framework and simulation setup. Section IV presents the results of the performance evaluation, and Section V concludes the study with a discussion of key findings and future research directions.

II. BACKGROUND

A. Precise Point Positioning model for deep-space

When post-processing spaceborne GNSS code and phase observations in PPP models, the ionosphere delay represents the dominant error contribution. While precise post-mission orbit/clock estimates available by the IGS analysis centers can be used, accurate total electron content (TEC) map lack validity because the pierce points of deep-space GNSS signals fall outside the well-calibrated regions of Earth-based ionospheric models [9]. A direct measurement of ionospheric path delay is possible from the combination of dual-frequency measurements. An ionosphere-free, dual-frequency PPP model

can benefit from the high precision of carrier-phase observables, which are primarily affected by the small carrier noise. However, its convergence is hindered by the poorer precision of code observables [12]. Additionally, this model requires tracking both frequencies from a given satellite, which is standard within the Terrestrial Service Volume (TSV). However, a receiver navigating outside the SSV often receives single-frequency signals from a particular satellite. This limitation arises due to the differing antenna patterns associated with each frequency, especially in the case of side lobes, which are the predominant tracking source for deep-space receivers [8], [13].

A SF combination of code and phase observables, the so-called GRAPHIC [10], can be formed where the ionospheric code delay compensates for the carrier-phase advance. The non-linear functional model of the GRAPHIC observation on frequency j , corrected for the ionosphere-free satellite clock δt_{IF}^s , can be expressed as

$$\begin{aligned} \frac{1}{2} (P_{r,j}^s + \Phi_{r,j}^s) + c\delta t_{IF}^s = & \|\mathbf{r}^s - \mathbf{r}_r\|_2 + c\tilde{\delta}t_{r,j} \\ & + \frac{\lambda_j}{2} (\tilde{N}_{r,j}^s + \omega_j) \\ & + \frac{1}{2} (\epsilon_{P,r,j}^s + \epsilon_{\Phi,r,j}^s) , \end{aligned} \quad (1)$$

where λ_j is the carrier wavelength and $\|\cdot\|_2$ the Euclidean norm. The following terms have been introduced:

- \mathbf{r}^s is the s -th GNSS satellite's center of mass position at signal emission time
- \mathbf{r}_r is the receiving antenna's reference point position at signal reception time
- $\tilde{\delta}t_{r,j} = \delta t_r + d_{r,j}$ is the receiver clock error (relative to GNSS system time) biased by the frequency-dependent receiver code hardware delay $d_{r,j}$
- $\tilde{N}_{r,j}^s$ is the estimable phase ambiguity bias
- ω_j is the phase wind-up term
- $\epsilon_{P,r,j}^s$ and $\epsilon_{\Phi,r,j}^s$ are the leftover terms which aggregate all non-systematic errors affecting code and phase observables, respectively

The geometry term in (1) assumes that the receiving antenna's phase center offsets and its variations have been compensated for through calibration. Similarly, GNSS satellite-specific calibration parameters are available from IGS antenna model products [14]. The estimable phase ambiguity bias can be further expanded

$$\tilde{N}_{r,j}^s = N_{r,j}^s + \frac{c}{\lambda_j} (\delta_j^s - d_j^s) - \frac{c}{\lambda} \frac{\mu_j}{\mu_{12}} \underbrace{(d_2^s - d_1^s)}_{DCB_{12}^s} \quad (2)$$

to recognize that the unknown integer-valued ambiguity $N_{r,j}^s$ is biased by the frequency-dependent satellite code d_j^s and phase δ_j^s hardware delays. The last term in (2), which involves the satellite-specific differential code bias (DCB), is omitted when corrections are applied based on IGS precise clock products. Using model-based wind-up compensation, the corrected GRAPHIC measurement can be written as

$$G_{r,j}^s = \|\mathbf{r}^s - \mathbf{r}_r\|_2 + c\tilde{\delta}t_{r,j} + \frac{\lambda_j}{2} \tilde{N}_{r,j}^s + \epsilon_{G,r,j}^s , \quad (3)$$

and this measurement must be processed similarly to carrier-phase observations. However, the residual error $\epsilon_{G,r,j}^s$ has a standard deviation which is roughly half that of code measurement noise [15].

For the orbit determination task, a SF-PPP model with GRAPHIC observations introduces the following set of unknown receiver states at t_k :

$$\boldsymbol{\xi}_k^\top = (\mathbf{r}_{r,k}^\top, \tilde{\delta}t_{r,j,k}) , \quad (4)$$

where the superscript \top denotes transposition. The receiver states are estimated together with the real-valued ambiguity bias $\tilde{N}_{r,j}$. The latter is constant across an arc of uninterrupted (i.e., without cycle slips) carrier tracking of a given satellite on an active receiver channel [15]. If a dual-constellation model is considered, (4) remains valid under the assumption of known (e.g., demodulated from the navigation message) inter-constellation timing bias.

B. Nonlinear least-squares formulation

The positioning model presented in Section II-A is solved as a LS problem. It consists of estimating the solution vector $\mathbf{x} \in \mathbb{R}^n$, with n denoting the number of unknown parameters, by minimizing the Euclidean norm squared of the residual vector function

$$\boldsymbol{\rho}(\mathbf{x}) = \mathbf{y} - \mathbf{f}(\mathbf{x}) , \quad (5)$$

where $\boldsymbol{\rho}(\mathbf{x}) \in \mathbb{R}^m$ and m is the number of available measurements. This residual represents the difference between the observed measurements \mathbf{y} and the predictive model $\mathbf{f}(\mathbf{x})$. The following optimization problem is solved [16], [17]:

$$\hat{\mathbf{x}}_{LS} = \arg \min_{\mathbf{x} \in \mathbb{R}^n} \Psi(\mathbf{x}), \quad \Psi(\mathbf{x}) = \frac{1}{2} \|\boldsymbol{\rho}(\mathbf{x})\|_2^2 , \quad (6)$$

where $\Psi(\mathbf{x})$ is the objective function to minimize and $\hat{\mathbf{x}}_{LS}$ its estimator. In this study, the LS problem is solved as a batch adjustment (with iterations) by simultaneously processing undifferenced observations from multiple consecutive epochs [9]. Given a batch of L epochs, t_1, \dots, t_L , the solution vector for the adopted SF-PPP model is defined as

$$\mathbf{x} = (\mathbf{X}^\top, \mathbf{N}^\top) = (\boldsymbol{\xi}_1^\top, \dots, \boldsymbol{\xi}_L^\top, \tilde{N}_1, \dots, \tilde{N}_B) , \quad (7)$$

where:

- $\mathbf{X} \in \mathbb{R}^{4L}$ combines the time-varying receiver states (cf. (4)) over the L epochs in the batch.
- $\mathbf{N} \in \mathbb{R}^B$ contains the ambiguity biases associated with B distinct active receiver tracking channels, each corresponding to the reception of a specific satellite signal on a given frequency. Every GRAPHIC observation in the batch has an ambiguity bias that maps to one of the parameters in \mathbf{N} .

Denoting by $k(i)$ the epoch index and by $\mu(i)$ the index of the ambiguity bias associated with the i -th corrected GRAPHIC observation in the batch, the predictive model $f_i(\mathbf{x})$ follows from (3):

$$f_i(\mathbf{x}) = \|\mathbf{r}_{k(i)}^s - \mathbf{r}_{r,k(i)}\|_2 + c\tilde{\delta}t_{r,j,k(i)} + \frac{\lambda_j}{2} \tilde{N}_{\mu(i)} , \quad (8)$$

$\tilde{N}_{\mu(i)}$ being relative to a specific satellite s on a given frequency j .

As a matter of fact, (8) defines a nonlinear relationship in \mathbf{x} through (4), thus making (6) a nonlinear LS problem. This type of problem is typically solved using the Newton method or one of its variants, such as the Gauss-Newton (GN) method [18], [19].

The GN method is an iterative algorithm that constructs a linear approximation of $\boldsymbol{\rho}(\mathbf{x})$. At each iteration p , the residual function is locally approximated via a first-order Taylor expansion about the current iterate solution $\hat{\mathbf{x}}^{(p)}$:

$$\boldsymbol{\rho}(\mathbf{x}) \simeq \boldsymbol{\rho}(\hat{\mathbf{x}}^{(p)}) + \hat{\mathbf{J}}_p \underbrace{(\mathbf{x} - \hat{\mathbf{x}}^{(p)})}_{\Delta \mathbf{x}^{(p)}} . \quad (9)$$

$\hat{\mathbf{J}}_p = \mathbf{J}_r(\hat{\mathbf{x}}^{(p)}) \in \mathbb{R}^{m \times n}$ is the Jacobian matrix of $\boldsymbol{\rho}(\mathbf{x})$ evaluated at $\hat{\mathbf{x}}^{(p)}$, and $\Delta \mathbf{x}^{(p)}$ represents the update step at the p -th iteration.

By substituting (9) into (6), the linearized LS problem takes the form:

$$\min_{\Delta \mathbf{x}^{(p)} \in \mathbb{R}^n} \Psi(\Delta \mathbf{x}^{(p)}), \quad \Psi(\Delta \mathbf{x}^{(p)}) = \frac{1}{2} \left\| \hat{\mathbf{J}}_p \Delta \mathbf{x}^{(p)} + \boldsymbol{\rho}(\hat{\mathbf{x}}^{(p)}) \right\|_2^2 \quad (10)$$

For the i -th observation, $\hat{\mathbf{J}}_p$ contains the partial derivatives of (8) with respect to \mathbf{x} :

$$\nabla_{\boldsymbol{\xi}_i}^\top = \delta_{k(i),l} \cdot \left(-\mathbf{e}_{r,k(i)}^{s\top}, c \right) \quad (11)$$

$$\frac{\partial f_i(\mathbf{x})}{\partial \tilde{N}_b} = \delta_{\mu(i),b} \cdot \frac{\lambda_j}{2} , \quad (12)$$

where δ denotes the Kronecker symbol and

$$\mathbf{e}_{r,k(i)}^{s\top} = \frac{\mathbf{r}_{k(i)}^s - \mathbf{r}_{r,k(i)}}{\|\mathbf{r}_{k(i)}^s - \mathbf{r}_{r,k(i)}\|_2} \quad (13)$$

is the unit line-of-sight vector from the receiving antenna's reference point position at signal reception time $t_{k(i)}$ to the GNSS satellite position at signal emission time.

The solution to (10) depends on the nature of the linear system $\hat{\mathbf{J}}_p \Delta \mathbf{x}^{(p)} = -\boldsymbol{\rho}(\hat{\mathbf{x}}^{(p)})$. If the system is *overdetermined* with a number of observations that exceeds or equals the number of unknowns (i.e., $m \geq n$) and $\hat{\mathbf{J}}_p$ has full (column) rank [20], then the following conditions hold [11]:

- $\hat{\mathbf{J}}_p$ has the trivial null space $\mathcal{N}\{\hat{\mathbf{J}}_p\} = \{\mathbf{0}\}$.
- $\hat{\mathbf{J}}_p^\top \hat{\mathbf{J}}_p$ is non-singular.

Consequently, (10) has unique minimizer

$$\Delta \mathbf{x}^{(p)} = (\hat{\mathbf{J}}_p^\top \hat{\mathbf{J}}_p)^{-1} \hat{\mathbf{J}}_p^\top \boldsymbol{\rho}(\hat{\mathbf{x}}^{(p)}) , \quad (14)$$

where $\hat{\mathbf{J}}_p^\dagger = (\hat{\mathbf{J}}_p^\top \hat{\mathbf{J}}_p)^{-1} \hat{\mathbf{J}}_p^\top$ is the well-known Moore-Penrose pseudoinverse of $\hat{\mathbf{J}}_p$, also known as the left pseudoinverse of $\hat{\mathbf{J}}_p$. The new approximation to the solution vector at iteration $p+1$ is then given by:

$$\hat{\mathbf{x}}^{(p+1)} = \hat{\mathbf{x}}^{(p)} + \Delta \mathbf{x}^{(p)} . \quad (15)$$

On the contrary, if the system is *underdetermined* (i.e., $m < n$) and $\hat{\mathbf{J}}_p$ has full (row) rank [20], then the null space of $\hat{\mathbf{J}}_p$ is non-trivial and (10) admits infinitely many solutions. A

common approach is to select the solution which minimizes the Euclidean norm of $\Delta \mathbf{x}^{(p)}$. This minimum-norm solution is

$$\Delta \mathbf{x}^{(p)} = \hat{\mathbf{J}}_p^\top (\hat{\mathbf{J}}_p \hat{\mathbf{J}}_p^\top)^{-1} \boldsymbol{\rho}(\hat{\mathbf{x}}^{(p)}), \quad (16)$$

where $\hat{\mathbf{J}}_p^\dagger = \hat{\mathbf{J}}_p^\top (\hat{\mathbf{J}}_p \hat{\mathbf{J}}_p^\top)^{-1}$ is the Moore-Penrose pseudoinverse in the case of full rank "fat" matrix, also known as the right pseudoinverse of $\hat{\mathbf{J}}_p$.

III. METHODOLOGY

A. Regularized least-squares with a-priori constraints

The conditioning of $\hat{\mathbf{J}}_p$ is a critical factor to monitor when solving (10). The condition number of the Jacobian, defined as the ratio between its largest and smallest non-zero singular values [18], provides insight into the sensitivity of the LS solution to perturbations in the input measurements. A matrix with a large condition number is said to be ill-conditioned, while a matrix with a small condition number is considered well-conditioned. This analysis considers ill-conditioning in matrices that are either rank-deficient or nearly rank-deficient. This includes cases where the matrix rank is strictly lower than the number of rows or columns, as well as cases where the matrix is numerically full-rank but exhibits nearly linear dependence among its rows or columns. Both conditions are particularly relevant when addressing GNSS-based kinematic OD in cis-lunar regime.

As highlighted in (11), the Jacobian matrix $\hat{\mathbf{J}}_p$ depends on the line-of-sight unit vectors between the receiving antenna and the GNSS satellites. As the S/C moves farther from Earth, these vectors become increasingly collinear, leading to an ill-conditioned Jacobian. Moreover, the normal equations for the SF-PPP model discussed in Section II-A are inherently rank deficient due to the linear dependence of the Jacobian's columns relative to clock offset and ambiguity bias [15], [21]. This rank deficiency persists regardless of the batch size employed in the LS adjustment, as it originates from the structure of the problem rather than the specific satellite geometry or scenario under analysis.

To tackle ill-conditioning, it is common to apply a regularization procedure to each GN iteration. Regularization involves adding a constraint to the objective function to transform the problem from ill-conditioned to well-conditioned [22]. In this analysis, Tikhonov's method is considered. It consists of adding a regularization term

$$\|\mathbf{L}(\mathbf{x} - \bar{\mathbf{x}})\|_2^2 \quad (17)$$

to the objective function of the linearized problem (10). The Tikhonov functional (17) introduces the following quantities:

- $\mathbf{L} \in \mathbb{R}^{q \times n}$ the regularization matrix ($q \leq n$). This matrix can take various forms, typically being either an identity matrix (i.e., $\mathbf{L} = \mathbf{I}_n$) or a diagonal weighting matrix.
- $\bar{\mathbf{x}}$ the a-priori solution vector.

When available, prior information about the receiver states and the ambiguity parameters can be incorporated into the regularized problem to favor solutions that do not deviate significantly from it. By linearizing (17) at the the current

LuGRE Phase	OP_ID	Orbital radius (RE)
Commissioning	OP_1	17.18
	OP_2	31.24
	OP_3	46.22
	OP_4	55.58
LLO	OP_5	61.19
	OP_6	63.56
MS	OP_7	63.24

TABLE I: Representative LuGRE datasets of GNSS payload operations across different mission phases and orbital altitudes, expressed in Earth radii (RE).

iterate solution $\hat{\mathbf{x}}^{(p)}$, the linearized objective function of the regularized LS problem (10) can be rewritten as [11]:

$$\begin{aligned} \Psi(\Delta \mathbf{x}^{(p)}) &= \frac{1}{2} \|\hat{\mathbf{J}}_p \Delta \mathbf{x}^{(p)} + \boldsymbol{\rho}(\hat{\mathbf{x}}^{(p)})\|_2^2 \\ &+ \frac{\lambda^2}{2} \|\mathbf{L}(\hat{\mathbf{x}}^{(p)} + \Delta \mathbf{x}^{(p)} - \bar{\mathbf{x}})\|_2^2, \end{aligned} \quad (18)$$

where $\lambda > 0$ is a regularization parameter that balances the contribution of the regularization term in the minimization of (18). The Tikhonov's functional in (18) overcomes the ill-conditioning caused by the inherent rank deficiency of $\hat{\mathbf{J}}_p$ by introducing a new LS problem with a new well-conditioned Jacobian matrix $\tilde{\mathbf{J}}_p = [\hat{\mathbf{J}}_p^\top, \lambda \mathbf{L}^\top]^\top$ having full rank [11], [23]. The assumption $\mathcal{N}(\tilde{\mathbf{J}}_p) \cap \mathcal{N}(\mathbf{L}) = \{\mathbf{0}\}$ that $\tilde{\mathbf{J}}_p$ has trivial null space leads to the unique minimizer of (18) in the overdetermined case [11]:

$$\begin{aligned} \Delta \mathbf{x}^{(p)} &= (\hat{\mathbf{J}}_p^\top \hat{\mathbf{J}}_p + \lambda^2 \mathbf{L}^\top \mathbf{L})^{-1} \hat{\mathbf{J}}_p^\top \boldsymbol{\rho}(\hat{\mathbf{x}}^{(p)}) \\ &- \lambda^2 \mathbf{L}^\top \mathbf{L}(\hat{\mathbf{x}}^{(p)} - \bar{\mathbf{x}}), \end{aligned} \quad (19)$$

A more general solution to (18) can be considered, which is valid for both overdetermined and underdetermined cases [11], [24]. This formulation is based on the GSVD, which is detailed in Appendix A.

Let the rank of $\hat{\mathbf{J}}_p$ be denoted as r_p . The update step at the p -th iteration is given by

$$\Delta \mathbf{x}^{(p)} = - \sum_{\kappa=n-r_p+1}^q \nu_\kappa \mathbf{w}_\kappa - \sum_{\kappa=q+1}^n g_{\kappa-\epsilon}^{(p)} \mathbf{w}_\kappa - \mathbf{W}_1 \hat{\mathbf{W}}_1 \hat{\mathbf{x}}^{(p)}, \quad (20)$$

where $\epsilon = \max(n - m, 0)$ and

$$\nu_\kappa = \frac{c_{\kappa-n+r_p} g_{\kappa-\epsilon}^{(p)} + \lambda^2 d_{\kappa-n+r_p}^2 z_\kappa^{(p)}}{c_{\kappa-n+r_p}^2 + \lambda^2 d_{\kappa-n+r_p}^2}. \quad (21)$$

Here, $\mathbf{g}^{(p)} = \mathbf{U}^\top \boldsymbol{\rho}(\hat{\mathbf{x}}^{(p)})$ and $\mathbf{z}^{(p)} = \mathbf{V}^\top (\hat{\mathbf{x}}^{(p)} - \bar{\mathbf{x}})$, with c and d defined in (23). Building upon \mathbf{W} as defined in (22), $\hat{\mathbf{W}}_1 \in \mathbb{R}^{(n-r_p) \times n}$ is composed by the first $n - r_p$ rows of \mathbf{W}^{-1} , while $\mathbf{W}_1 \in \mathbb{R}^{n \times (n-r_p)}$ consists of the first $n - r_p$ columns of \mathbf{W} .

LuGRE phase		Commissioning		Transit		Low Lunar orbit (LLO)		Moon surface (MS)
OP_ID		OP_1 (17.18 RE)	OP_2 (31.24 RE)	OP_3 (46.22 RE)	OP_4 (55.58 RE)	OP_5 (61.19 RE)	OP_6 (63.56 RE)	OP_7 (63.24 RE)
GPS+Galileo Visibility	Min	5	4	5	5	5	4	4
	Max	30	21	12	12	9	6	10
	Mean	24.68	11.40	9.35	9.39	7.08	5.40	6.97
GDOP	Min	39.66	143.24	407.62	837.17	1152.57	1230.83	1682.23
	Max	148.86	94957.31	5141583.58	6070.41	34703.65	7488.11	4984.90
	Mean	48.67	295.66	742.28	1489.46	2540.96	2826.53	1915.70

TABLE II: Summary statistics of GNSS radiometric visibility and dilution of precision (DOP) for the representative LuGRE datasets.

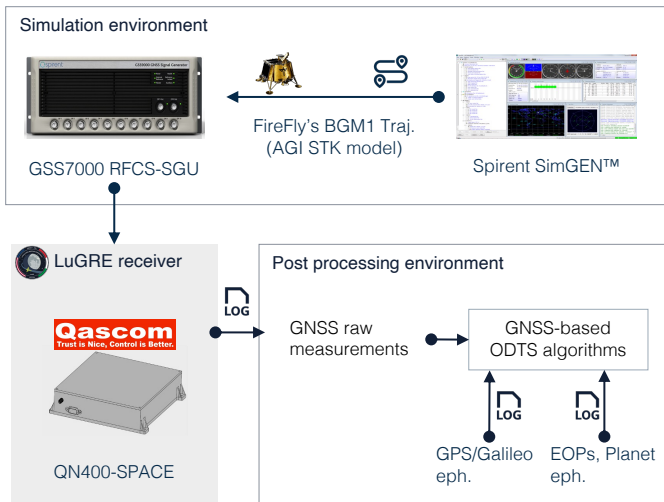


Fig. 1: Simulation testbed with HIL for preliminary navigation experiments using GNSS data from the LuGRE receiver.

B. Simulation Framework

The ongoing LuGRE mission is considered as case-study to assess the performance of the regularized batch estimator in solving the kinematic OD problem using GRAPHIC observations. As part of National Aeronautics and Space Administration (NASA)'s Commercial Lunar Payload Services (CLPS) program (Task Order 19D), LuGRE is a technology demonstration payload developed by NASA's Exploration Systems Development Mission Directorate (ESDMD) in collaboration with the Italian Space Agency (ASI) [6], [7]. The payload, carried aboard Firefly's BGM1 lander, features the Navigation Early Investigation on Lunar surface (NEIL) module, a spaceborne GNSS Software Defined Radio (SDR) receiver designed for navigation in cis-lunar space and on the Moon.

A simulation campaign was conducted using a Spirent GSS7000 GNSS Radio Frequency (RF) constellation simulator [25], configured to accurately replicate the operational conditions of the GNSS payload across different mission phases. The testbed, operating in a HIL configuration, was deployed as a ground-segment tool for preparatory navigation experiments with GNSS data from the LuGRE receiver, enabling

performance evaluation under controlled yet representative conditions. The overall simulation setup and its components are illustrated in Figure 1.

To model the GNSS signal environment, a GPS-Galileo scenario was set up in Spirent SimGEN™ software, consistent with the receiver's dual-band, dual-constellation design specifications [26]. The latest Almanac data and space-segment operational advisories were incorporated into the navigation system configuration to ensure realistic satellite ephemerides. For the Global Positioning System (GPS) constellation, the gain patterns for batches IIR and IIR-M were modeled following the specifications in [27], with the boresight EIRP calibrated based on [28] for L1 C/A and L5-Q signals. Similarly, the gain pattern for batch IIF was derived from [29] and applied to batch III-A. In the case of the Galileo constellation, the antenna radiation patterns were configured according to the model in [30]. Additionally, the modeled signals for both GPS and Galileo were subject to an off-boresight mask to account for satellite body effects, ensuring a realistic representation of non-isotropic radiation patterns. Further details on the RF link simulation methodology are available in [26].

The BGM1 lander's trajectory, based on a pre-launch orbit design, was imported into Ansys Systems Tool Kit (STK) and processed with the High Precision Orbit Propagator (HPOP) to generate refined position and velocity states for the entire mission. From this trajectory, representative segments at varying altitudes and mission phases were selected to assess payload performance under different multilateration geometries and satellite radiometric visibility conditions. Table I reports the list of the analyzed datasets, covering multiple LuGRE operations across four mission phases: Commissioning, Transit, low lunar orbit (LLO), and Moon surface (MS). For each selected operation, Spirent SimGEN™ software generated high-fidelity digital signals for GPS L1/L5 and Galileo E1/E5a bands. During each test, the GNSS payload operated in real-time, logging dual-band, dual-constellation code and phase observables for post-processing.

IV. RESULTS

A. Navigation analysis

The expected navigation performance of the GNSS payload across the representative LuGRE operational phases (cf. Ta-

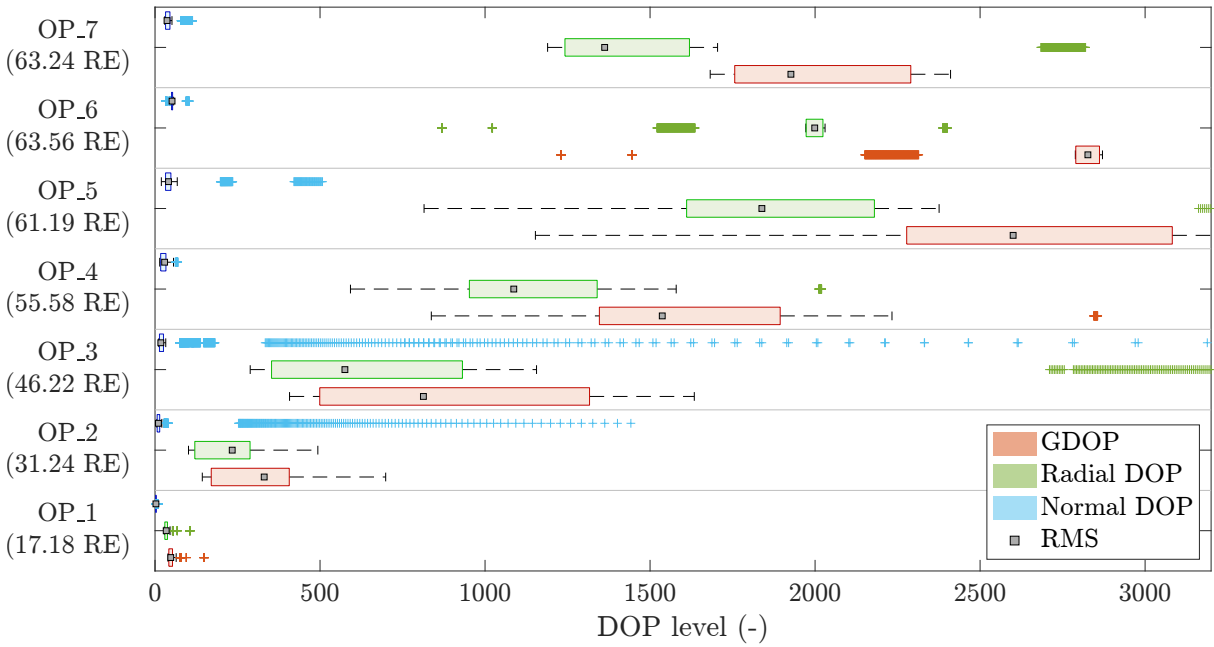


Fig. 2: Boxplot of DOP metrics for each representative dataset. Three metrics are illustrated: Geometric Dilution Of Precision (GDOP), radial DOP, and normal DOP.

ble I) is assessed by analyzing radiometric visibility indices and meaningful DOP metrics.

Table II reports summary radiometric visibility statistics for combined GPS and Galileo constellations across the analyzed operations. A clear trend of decreasing average satellite availability can be observed as the payload receiver transitions from lower MTO altitudes to the lunar regime, including the LLO phase and the surface scenario. This decreasing trend is also reflected in the maximum number of simultaneously tracked satellites for each representative dataset, although the minimum number of tracked satellites remains relatively consistent across all operational windows. An exception to the overall trend is observed when comparing OP_6 with OP_7, where the latter records a slightly higher mean number of satellites. This inversion may result from increased lunar occultation effects when the S/C travels certain LLO segments, reducing visibility compared to the more stable conditions during surface operations. Furthermore, discrepancies in the simulation model, such as misrepresentation of lunar topography and planetary dynamics, might lead to an overestimation of satellite visibility compared to what is seen in real operations.

Table II also reports summary statistics of GDOP, which allow to characterize the geometry of the GNSS-based multilateration problem. On the average, a GDOP increase is observed across the representative datasets at increasing orbital altitudes. For instance, the mean GDOP rises from 48.67 in OP_1 to 1489.46 in OP_4, and further to 2540.96 and 2826.53 for OP_5 and OP_6, respectively, in LLO. However, the representative dataset for surface operations exhibits an average GDOP which is significantly lower than that of OP_6 in LLO and only 22.25% higher than the value for

OP_4 in Transit. The geometry improvement in OP_7 can be attributed to the more stable satellite visibility conditions and the reduced dynamics when the receiver is stationary on the lunar surface. The discussed mean GDOP statistics were computed after filtering outliers, defined as estimates more than 1.5 interquartile ranges above the upper quartile (i.e., 75-th percentile (pct)) or below the lower quartile (i.e., 25-th pct). In fact, it is worth noting that the maximum GDOP values recorded for some datasets, especially OP_2 and OP_3, can be considered outliers if compared to the average sample statistic. This phenomenon was already observed in [31] for a LLO scenario, which highlighted a DOP profile characterized by abrupt discontinuities and steep ascending ramps. The minimum GDOP statistics of Table II, on the other hand, follow a pattern similar to the average statistic.

Additional characterization of the multilateration geometry is provided in Figure 2, which shows cumulative statistics of GDOP along with two additional DOP metrics: radial DOP and normal DOP, all referenced to a radial, in-track, cross-track (RIC) orbital frame. The radial DOP represents the component aligned with the S/C's instantaneous inertial position vector within the orbital plane, while the normal DOP combines the in-track and cross-track components, which lie in the plane defined by the angular momentum vector. In cis-lunar space and at lunar altitudes, the multilateration problem is largely dominated by radial geometry. This is primarily due to the limited spatial diversity among GNSS satellites, which results in increasing collinearity of the receiver-to-satellite line of sight (LOS) vectors. This is particularly evident in the skyplot visualizations of Figure 3, where elevation grids are reduced around the receiving antenna boresight (i.e., 90°

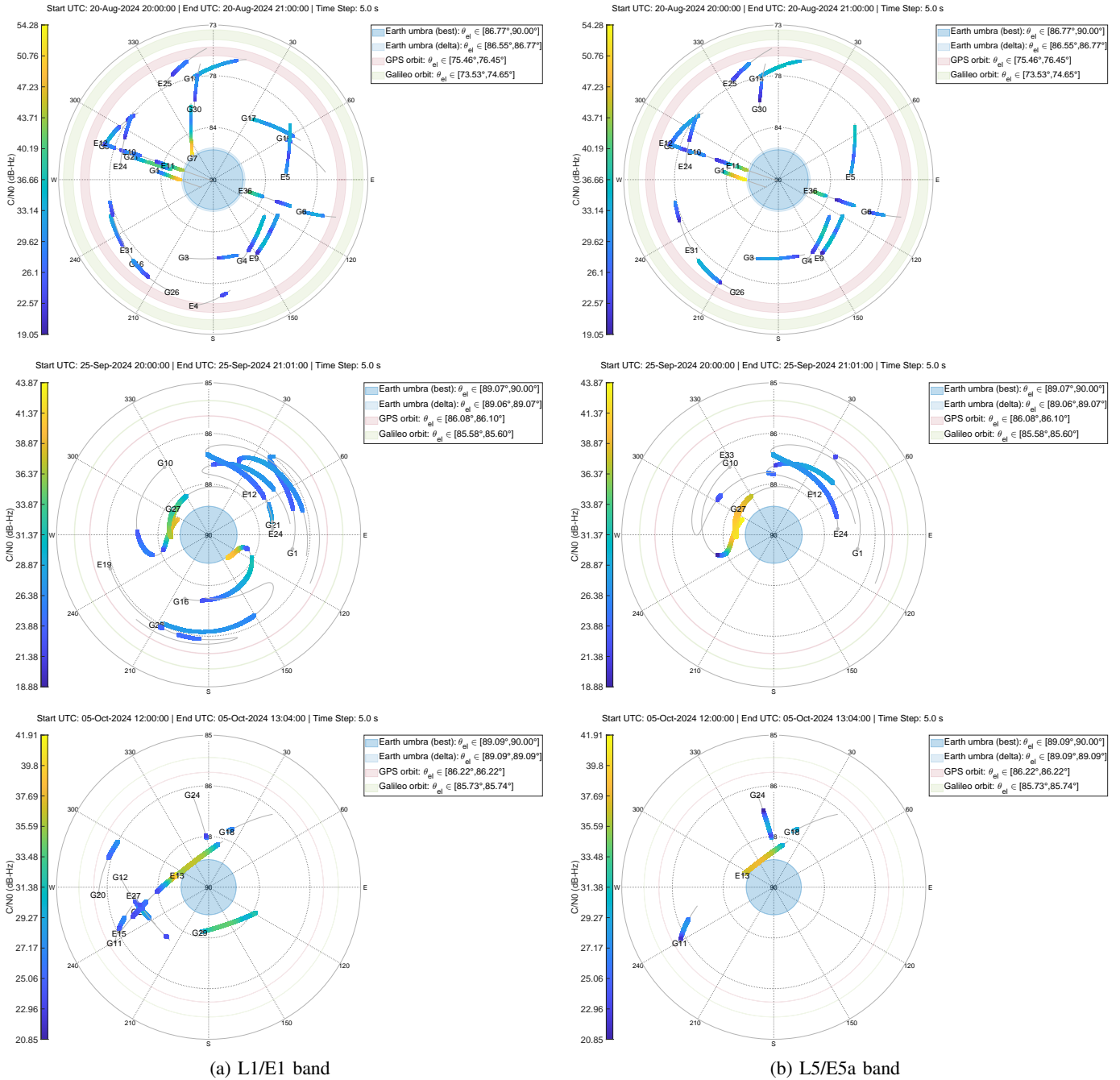


Fig. 3: Space skyplot of tracked GPS and Galileo satellites in RIC orbital frame for three representative LuGRE datasets: OP_1 (top row), OP_5 (middle row), and OP_7 (bottom row).

elevation). Such condition of collinearity makes radial position estimation particularly challenging as it strongly correlates with the estimation of the clock bias, thereby degrading the conditioning of the multilateration problem.

To further characterize the GNSS operational conditions of the LuGRE payload, Figure 3 presents the skyplot in a local orbital frame (i.e., a space skyplot) for three representative datasets covering the different mission phases: OP_1 (Transit), OP_5 (LLO), and OP_7 (MS). This polar diagram considers

the instantaneous relative dynamics between the S/C and the GNSS satellites, where satellite positions and velocities are projected onto a Local Vertical Local Horizontal (LVLH) frame [32]. The latter frame has the radial direction along the receiving antenna's boresight, assuming perfect pointing to the Earth's center of mass. The Earth's disk occupation and the elevation isolines of both GPS and Galileo orbits are also illustrated in the diagram, with a continuous patch representation which accounts for elevation variations across the dataset

epochs. Moreover, the dynamic trajectory of each satellite is overlaid with a heatmap of the estimated Carrier-to-Noise-density ratio (C/N_0) when signals on the L1/E1 band (left diagram) and on the L5/E5a band (right diagram) are tracked. The C/N_0 distribution reveals “hot zones” with higher signal strength near the Earth’s disk, indicating main lobe signal tracking from satellites either rising (i.e., entering radiometric visibility) or setting (i.e., gradually losing signal lock due to Earth blockage). In contrast, lower elevation regions in the skyplot exhibit weaker C/N_0 values, suggesting predominant tracking of side lobes. A threshold of approximately 30 dB-Hz can serve as a reasonable qualitative discriminator between main and side lobe tracking. As expected, side lobe signals dominate the cis-lunar regime, largely contributing to positioning availability.

Comparing the space skyplots between different bands for the same dataset, L5/E5a signals exhibit higher C/N_0 estimates, reaching up to 54 dB-Hz in OP_1 and up to 43 dB-Hz in OP_5 for GPS L5. This can be attributed to the broader beamwidth of L5/E5a transmission patterns and the lower path loss [28]. However, despite the higher signal strength, fewer L5/E5a signals are tracked overall, as only a subset of satellites in each constellation broadcasts signals on these lower-frequency bands. Additionally, GPS satellites are tracked more frequently than Galileo, likely due to the conservative modeling of Galileo’s Effective Isotropic Radiated Power (EIRP) in the simulation or its reduced spatial diversity, with satellites distributed across three orbital planes compared to GPS’s six.

B. Positioning performance and availability analysis

To assess the effectiveness of the proposed method, all simulations use a fixed batch length of 5 epochs. Table III reports the availability of PVTs solutions, along with the percentage of underdetermined cases in various cislunar scenarios. The row labeled *Minimum satellite vehicles (SVs) batch* specifies the minimum number of simultaneously tracked satellites required for a batch to be considered in the single-point PVT estimation (note that multi-band signals from the same satellite are counted as one). Batches that do not meet this requirement are excluded from the analysis, and no kinematic orbit solution is computed for the corresponding epochs. In the analyses, the considered values for the minimum number of SVs per batch are 2, 3, and 4. The third and fourth rows of Table III report, for each of these values, the percentage of epochs with an available PVT solution and the percentage of those that are underdetermined due to insufficient measurement redundancy collected within the batch. It is worth noting that, in short-batch SF-PPP models, having at least four tracked satellites does not necessarily ensure an overdetermined nonlinear LS problem. While two epochs are typically sufficient for overdeterminedness in terrestrial scenarios, this condition may not hold in deep-space environments due to limited satellite visibility.

The values in the table show that, for the first three representative datasets (OP_1, OP_2, and OP_3) corresponding to

the commissioning and transit mission phases, there is little difference in performance across LS batches with varying minimum SV thresholds. The availability percentages are nearly identical, and the occurrence of underdetermined PVT solutions is minimal. This indicates that the condition of having at least four continuously tracked satellites over the batch length is generally satisfied in all these datasets.

Beyond 50 Earth radii, a different trend emerges. Here, the benefits of relaxing the minimum SVs per batch requirement become more evident, particularly during the LLO and MS mission phases. In such scenarios, the stringent enforcement of the condition of four continuously tracked satellites often results in a considerable decline in the availability of solutions, reaching as low as 33.67% for OP_6 in LLO. Conversely, the relaxation of the threshold to three, or even two, SVs has been shown to significantly enhance the availability, with a consistent exceedance of 87% across all cislunar regimes. It should be noted, however, that this improvement is at the cost of a higher incidence of underdetermined solutions. This highlights the importance of using a kinematic estimator capable of handling both overdetermined and underdetermined cases, thus ensuring solution availability under varying conditions. Table IV shows the performance of the OD in terms of radial and in-track errors for both position and velocity. The second row reports the a-priori constraints applied to the receiver state. In a realistic operational scenario, one could expect an initial a-priori constraint to be uplinked as a ground telecommand to support a cold start of the algorithm. Subsequent batches would then be initialized using the solution from the previous one. However, in the following analysis, to ensure a controlled and repeatable evaluation of the estimator’s performance, OD error statistics are assessed under different levels of a-priori accuracy. Specifically, three sets of a-priori constraints are considered, introducing synthetic errors with respect to the ground truth: 100 km in position and 100 m/s in velocity, 10 km and 10 m/s, and finally 1 km and 1 m/s. For each case, the regularization matrix \mathbf{L} was constructed through the Cholesky factorization of the covariance matrix associated with the corresponding a-priori constraint.

It is also important to note that, in contrast to position estimation which is based on the regularised GN method, velocity is computed separately in a single step. Specifically, the Jacobian matrix from the final GN position solution is used within a regularized model to estimate velocity from Doppler measurements.

From Table IV, it can be observed that with a minimum of three tracked satellites per batch, the estimator generally achieves stable performance in both the radial and normal components, largely regardless of the magnitude of the a-priori error. This holds true as long as the receiver clock bias is constrained within a few milliseconds. However, when the radiometric visibility threshold is relaxed to two satellites, the estimator becomes more sensitive to the a-priori error, particularly in the normal component. For example, in OP_5, the 95-th pct normal position error exceeds 40 km for a 10 km prior error, indicating that the estimator may converge

to a local minimum of the objective function that does not correspond to the true receiver state. A similar outcome is observed in OP_6. Notably, the gap between the 75-th pct and 95-th pct statistics is substantial, as the former typically exclude most batches with only two visible SVs. This behavior is most evident in LLO scenarios, which, as shown in Table III, more frequently satisfy the condition of having only two satellites per batch.

In contrast, a different trend is observed for the velocity estimates (Table V), which appear highly sensitive to inaccurate a-priori constraints across all cislunar scenarios.

Overall positioning performance degrades in datasets OP_4 to OP_6 compared to lower-altitude transit segments, mainly due to reduced satellite visibility (Table III) and unfavorable GDOP conditions (2). Despite this, results remain encouraging even under worst-case a-priori constraints, provided at least three satellites are tracked. Notably, in OP_6 the 95-th pct radial error reaches 1351.31 m at lunar orbit apogee. This is comparable to the accuracy achieved by a Unscented Kalman Filter (UKF)-based dynamic OD solution at similar altitudes in [31]. Similarly, the worst-case normal error remains under 400 m. Velocity estimation errors are generally larger, especially when compared to those obtained with the UKF-based approach presented in [31]. The worst performance is observed in OP_5, where the radial velocity error reaches 5.99 m/s and the normal component peaks at 26 m/s under the worst-case *a-priori* velocity constraint. Overall, relaxing the radiometric visibility requirement to a minimum of two satellites per batch yields acceptable positioning performance at the 95-th pct below 50 RE, but leads to significant degradation in LLO. An exception is the MS dataset, where the radial error remains as low as 16.78 m, even under a 100 km position constraint. As for velocity, radial errors stay within 6 m/s across all datasets. However, normal velocity errors in LLO remain large unless a highly accurate velocity constraint is provided. These findings highlight the importance of tailored *a-priori* constraints and visibility conditions to ensure reliable OD performance in cislunar missions.

V. CONCLUSION

This study has demonstrated the performance of the SF-PPP model for kinematic OD in a cislunar environment using GRAPHIC measurements. A regularized LS batch approach was investigated to assess its potential in terms of both solution availability and position and velocity error. The ongoing LuGRE mission was considered as a case study to evaluate the effectiveness of the regularized batch estimator in solving the kinematic OD problem.

The algorithm was tested through post-processing of raw multi-band GPS/Galileo observables, generated by the NEIL receiver in a HIL test. The evaluated datasets covered a wide range of distances from Earth, spanning from 17.18 to 63.24 RE.

The core of the method relies on solving a nonlinear LS problem regularized with Tikhonov regularization. The regularization term incorporates both a regularization matrix

and a-priori receiver state information. The problem is solved iteratively, similar to the traditional GN method, but using a GSVD-based formulation [11] that enables handling both overdetermined and underdetermined cases.

Performance assessment was conducted by analyzing position and velocity estimation errors across three different levels of initial state uncertainty and three minimum satellite constraints (2, 3, and 4 satellites in the LS batch). The key results obtained are as follows:

- From an availability perspective, the algorithm effectively managed underdetermined cases, ensuring solution availability above 89% in most datasets when the radiometric visibility threshold of three satellites was assumed.
- From a positioning and velocity standpoint, the regularized estimator demonstrated promising accuracy across the cislunar scenarios, especially when at least three satellites were tracked per batch and the receiver clock bias was properly constrained. Under these conditions, the estimator showed strong robustness to biases in the a-priori constraint, with 95th-pct position errors staying below 1.4 km in the radial direction and 400 m in the normal direction across all datasets. Velocity errors showed greater sensitivity to a-priori uncertainty. In the worst-case scenario, errors reached up to 6 m/s (radial) and 26 m/s (normal). However, assuming a prior velocity error of just 1 m/s significantly improved performance, keeping velocity errors below 4.5 m/s and 2.6 m/s in the radial and normal directions, respectively.

Overall, the SF-PPP model for kinematic OD, combined with a regularized LS algorithm capable of handling both overdetermined and underdetermined conditions, has demonstrated promising performance in terms of both availability and positioning accuracy. Future research will focus on improving the positioning algorithm and further validating its performance using real mission datasets collected during the LuGRE mission.

ACKNOWLEDGMENT

This study was funded within the contract n. 2021-26-HH.0 ASI/Politecnico di Torino "Attività di R&S inerente alla Navigazione GNSS nello Space volume Terra/Luna nell'ambito del Lunar GNSS Receiver Experiment". The authors would like to thank Qascom for supplying the representative datasets of LuGRE operations that supported this study.

APPENDIX

A. Generalized Singular Value Decomposition (GSVD)

Consider two matrices $\mathbf{J} \in \mathbb{R}^{m \times n}$ and $\mathbf{L} \in \mathbb{R}^{q \times n}$ with ranks r and q , respectively. The GSVD of the matrix pair (\mathbf{J}, \mathbf{L}) is a matrix decomposition of the form [11]

$$\mathbf{J} = \mathbf{U}\Sigma_{\mathbf{J}}\mathbf{W}^{-1}, \quad \mathbf{L} = \mathbf{V}\Sigma_{\mathbf{L}}\mathbf{W}^{-1}, \quad (22)$$

where $\mathbf{U} \in \mathbb{R}^{m \times m}$ and $\mathbf{V} \in \mathbb{R}^{q \times q}$ are matrices with orthonormal columns \mathbf{u}_{κ} and \mathbf{v}_{κ} , and $\mathbf{W} \in \mathbb{R}^{n \times n}$ is a nonsingular matrix with columns \mathbf{w}_{κ} .

LuGRE Phase	Commissioning				Transit				Low Lunar Orbit (LLO)				Moon Surface (MS)																			
OP_ID	OP_1 (17.18 RE)				OP_2 (31.24 RE)				OP_3 (46.22 RE)				OP_4 (55.58 RE)				OP_5 (61.19 RE)				OP_6 (63.56 RE)				OP_7 (63.24 RE)							
Minimum SVs batch	2	3	4		2	3	4		2	3	4		2	3	4		2	3	4		2	3	4		2	3	4		2	3	4	
PVT availability (%)	99.27	99.27	99.27		94.29	93.51	92.74		93.86	93.60	93.60		94.81	89.89	84.15		99.86	92.75	83.33		87.96	69.65	33.67		87.96	69.65	33.67		99.08	97.51	83.97	
PVT undetermined (%)	0.029	0.029	0.029		2.37	1.55	0.73		0.30	0.027	0.027		5.33	0.15	0.16		16.55	10.15	0		69.07	60.93	19.19		69.07	60.93	19.19		15.78	14.42	0.63	

TABLE III: Percentage of available PVT solutions and undetermined multi-epoch batches across representative LuGRE datasets. Statistics are evaluated for varying minimum visibility thresholds (unique SVs) in the multi-epoch batch.

LuGRE Phase	Commissioning				Transit				Low Lunar Orbit (LLO)				Moon Surface (MS)																			
OP_ID	OP_1 (17.18 RE)				OP_2 (31.24 RE)				OP_3 (46.22 RE)				OP_4 (55.58 RE)				OP_5 (61.19 RE)				OP_6 (63.56 RE)				OP_7 (63.24 RE)							
A-priori position (km) and velocity (m/s) error	100, 100	10, 10	1, 1		100, 100	10, 10	1, 1		100, 100	10, 10	1, 1		100, 100	10, 10	1, 1		100, 100	10, 10	1, 1		100, 100	10, 10	1, 1		100, 100	10, 10	1, 1		100, 100	10, 10	1, 1	
Radial position error (m)	41.01	41.01	41.06		18.20	18.21	18.19		9.28	9.28	9.29		7.43	7.44	7.49		7.88	7.87	7.85		757.74	757.73	755.69		262.91	262.94	263.31		3.31	3.30	3.28	
95-th pct. (m)	71.05	71.03	71.17		35.94	35.96	36.00		16.07	16.05	16.09		19.82	19.79	19.76		1066.80	1066.77	1066.21		335.81	335.76	335.94		7.25	7.22	7.21					
Position error (m)	138.03	138.04	138.12		69.56	69.53	69.20		34.54	34.54	34.58		35.06	35.00	34.84		1355.34	1355.37	1355.36		397.21	397.16	396.93		15.43	15.43	15.41					
Normal position error (m)	8.04	8.04	8.04		45.12	45.09	45.01		81.54	81.54	81.52		122.20	122.22	122.55		91.04	91.23	90.90		144.61	144.12	143.67		80.75	80.77	80.75					
95-th pct. (m)	13.04	13.04	13.07		88.95	88.79	88.57		121.28	121.28	121.41		229.31	230.22	230.66		335.49	333.98	335.82		429.99	431.33	423.00		201.92	202.19	204.74					
Radial position error (m)	41.01	41.01	41.06		18.20	18.21	18.19		9.28	9.28	9.29		7.43	7.44	7.49		7.88	7.87	7.85		757.74	757.73	755.69		262.91	262.94	263.31		3.31	3.30	3.28	
95-th pct. (m)	71.05	71.03	71.17		35.74	35.77	35.71		16.07	16.05	16.09		18.21	18.18	18.13		1024.24	1024.25	1024.09		257.54	257.59	257.57		6.73	6.71	6.66					
Normal position error (m)	5.42	5.42	5.42		26.75	26.71	26.75		60.41	60.40	60.39		83.15	83.30	83.01		93.46	93.83	94.52		133.37	132.90	134.51		81.50	81.57	81.50					
95-th pct. (m)	8.04	8.04	8.04		45.66	45.62	45.64		81.54	81.54	81.52		128.59	128.62	128.77		147.59	147.73	147.74		219.34	218.72	223.69		124.26	124.26	124.57					
Radial position error (m)	41.01	41.01	41.06		18.43	18.42	18.25		9.30	9.29	9.27		7.99	7.98	7.73		622.16	599.12	598.52		173.73	42.59	40.16		3.01	2.99	2.91					
95-th pct. (m)	71.05	71.03	71.17		36.47	36.35	35.77		16.13	16.14	16.13		21.79	21.53	19.18		997.74	993.24	993.14		336.78	236.48	229.97		6.99	6.83	6.66					
Normal position error (m)	138.03	138.04	138.12		72.70	72.13	69.46		35.40	35.18	34.55		59.66	47.04	35.15		1349.03	1348.88	1348.24		1386.52	376.23	373.67		16.78	15.61	14.81					
95-th pct. (m)	5.42	5.42	5.42		27.00	27.00	26.95		60.53	60.51	60.67		87.24	87.28	87.52		98.83	98.81	99.50		172.16	171.47	164.71		82.13	82.37	81.50					
Radial position error (m)	13.04	13.04	13.07		96.94	97.11	96.39		122.00	122.04	122.00		2223.82	653.08	403.74		40663.41	4068.17	716.17		124690.00	12470.41	1250.13		292.24	294.62	239.43					
95-th pct. (m)	13.04	13.04	13.07		96.94	97.11	96.39		122.00	122.04	122.00		2223.82	653.08	403.74		40663.41	4068.17	716.17		124690.00	12470.41	1250.13		292.24	294.62	239.43					

TABLE IV: Position estimation statistics across representative LuGRE datasets. For each payload operation, cumulative errors are reported at the 50th, 75th, and 95th pct. in both radial and normal components of a RIC orbital frame. Statistics are evaluated for varying minimum visibility thresholds (unique SVs) in the multi-epoch batch.

LuGRE Phase OP_ID	Commissioning OP_1 (17.18 RE)			Transit OP_3 (46.22 RE)			OP_4 (55.58 RE)			Low Lunar Orbit (LLO) OP_6 (63.56 RE)			Moon Surface (MS) OP_7 (63.24 RE)								
	100	10	1, 1	100	10	1, 1	100	10	1, 1	100	10	1, 1	100	10	1, 1						
A-priori position (km) and velocity (m/s) error	2.04	2.01	1.50	2.04	2.01	1.50	2.01	1.98	1.49	2.05	2.00	1.50	2.15	2.11	1.58	1.98	1.95	1.45	2.03	2.00	1.50
Radial velocity error (m/s)	3.41	3.37	2.53	3.40	3.36	2.51	3.39	3.35	2.52	3.40	3.34	2.52	3.63	3.58	2.68	3.36	3.33	2.46	3.41	3.36	2.53
Normal velocity error (m/s)	5.77	5.70	4.22	5.75	5.67	4.27	5.79	5.70	4.24	5.73	5.67	4.24	6.01	5.92	4.48	5.79	5.70	4.27	5.76	5.68	4.19
Min 4 SVs batch	0.49	0.50	0.46	1.89	1.81	1.04	2.86	2.65	1.15	4.19	3.55	1.20	5.30	4.00	1.19	6.13	4.10	1.19	5.66	4.28	1.18
Min 3 SVs batch	0.73	0.73	0.67	2.90	2.73	1.50	4.19	3.78	1.65	6.37	5.28	1.70	8.18	5.79	1.68	9.36	6.00	1.65	8.20	6.24	1.71
Min 2 SVs batch	1.22	1.22	1.06	5.00	4.55	2.29	6.94	6.14	2.49	13.13	8.64	2.62	19.30	9.50	2.53	15.97	9.02	2.43	13.36	9.49	2.50
Radial velocity error (m/s)	2.04	2.01	1.50	2.03	2.01	1.50	2.01	1.98	1.49	2.01	1.99	1.49	2.11	2.08	1.56	2.08	2.03	1.52	2.00	1.97	1.47
Normal velocity error (m/s)	3.41	3.37	2.53	3.39	3.36	2.52	3.39	3.35	2.52	3.38	3.33	2.53	3.66	3.59	2.66	3.41	3.36	2.51	3.39	3.35	2.51
Min 3 SVs batch	5.77	5.70	4.22	5.82	5.68	4.23	5.79	5.70	4.24	5.74	5.65	4.23	5.99	5.92	4.46	5.73	5.70	4.32	5.75	5.67	4.26
Min 2 SVs batch	0.49	0.50	0.46	1.90	1.82	1.04	2.86	2.65	1.15	4.38	3.61	1.19	5.50	3.97	1.19	6.79	4.43	1.15	5.72	4.29	1.20
Radial velocity error (m/s)	0.73	0.73	0.67	2.93	2.76	1.48	4.19	3.78	1.65	6.78	5.22	1.70	8.72	5.85	1.67	10.43	6.38	1.63	8.42	6.15	1.66
Normal velocity error (m/s)	1.22	1.22	1.06	5.10	4.64	2.26	6.94	6.14	2.49	17.44	8.79	2.60	26.07	9.17	2.47	17.98	9.73	2.45	15.56	9.54	2.43
Min 3 SVs batch	2.04	2.01	1.50	2.01	1.99	1.50	2.01	1.98	1.49	2.05	2.02	1.50	2.14	2.09	1.56	2.05	2.00	1.50	2.01	1.97	1.47
Normal velocity error (m/s)	3.41	3.37	2.53	3.42	3.36	2.51	3.38	3.34	2.52	3.38	3.34	2.52	3.65	3.58	2.65	3.48	3.38	2.53	3.40	3.35	2.51
Min 2 SVs batch	5.77	5.70	4.22	5.79	5.69	4.23	5.74	5.70	4.25	5.75	5.64	4.24	6.06	5.94	4.45	5.89	5.71	4.25	5.81	5.73	4.26
Radial velocity error (m/s)	0.49	0.50	0.46	1.92	1.82	1.04	2.88	2.66	1.16	4.60	3.67	1.21	5.88	4.03	1.17	8.25	4.65	1.16	5.80	4.30	1.20
Normal velocity error (m/s)	0.73	0.73	0.67	2.97	2.78	1.48	4.22	3.82	1.65	7.36	5.38	1.72	9.89	6.00	1.66	15.16	6.70	1.66	8.64	6.16	1.66
Min 2 SVs batch	1.22	1.22	1.06	5.27	4.78	2.25	6.97	6.15	2.44	26.35	9.07	2.59	49.72	9.40	2.48	59.68	10.44	2.43	17.36	9.36	2.43

TABLE V: Velocity estimation statistics across representative LuGRE datasets. For each payload operation, cumulative errors are reported at the 50th, 75th, and 95th percs in both radial and normal components of a RIC orbital frame. Statistics are evaluated for varying minimum visibility thresholds (unique SVs) in the multi-epoch batch.